

Optical and thermal characterization of a variable geometry concentrator using ray-tracing tools and experimental data

Ramon Pujol-Nadal^{*1}, Víctor Martínez-Moll¹, Fabienne Sallaberry² and Andreu Moilà-
Pol¹

^{*} Tel: 34 – 971259542, Fax: 34 – 971173426, ramon.pujol@uib.es

¹Departament de Física, Universitat de les Illes Balears, Ctra de Valldemossa km 7,5,
07122, Palma de Mallorca, Illes Balears (Spain)

² CENER (National Renewable Energy Center), Solar Thermal Energy Department, C/
Ciudad de la Innovación, 7; 31621 Sarriguren, Navarra (Spain)

Abstract

Ray-tracing tools are commonly used to optically characterize solar concentrators, but the International Standards used to certify collectors for heating do not allow the use of these tools to analyse the optical behaviour of solar thermal systems. Solar concentrators for the medium temperature range often are of large dimensions and cannot be easily reoriented to the sun without an expensive rotating test platform suggested by the International Standards; therefore, some deficiencies can be detected if the standards procedures are applied to these types of concentrating collectors. In this paper, the use of ray-tracing tools combined with thermal experimental data is proposed to determine the energy balance coefficients by a Weighted Least Square adjustment

(WLS). The main advantages of this methodology are that the measurement of the thermal efficiency at normal incidence and solar concentrator reorientation are not required, the optical behaviour of the system can be determined for any position of the sun, and it can be used for in situ measurements for large-scale solar thermal collectors.

Keywords: Standard collector testing; Variable geometry; IAM; Ray-tracing; In situ measurements; Solar concentrator.

Nomenclature

α : solar absorptance of the absorber tube (-).

η_{ob}^{opt} : optical efficiency of the collector relative to beam solar radiation (-)

η_{od}^{opt} : optical efficiency of the collector relative to solar diffuse radiation (-)

θ_i : incidence angle (°)

θ_L : longitudinal incidence angle (°)

θ_T : transversal incidence angle (°)

ρ : reflectance of the reflector (-)

σ : standard deviation combining all optical errors (mrad)

A_a : aperture area of the collector (m²)

b_i : fitting parameters

C_a : ratio of collector and receiver apertures (-)

c_1 : heat loss coefficient respect to $(t_m - t_a) = 0$ K (Wm⁻²K⁻¹)

c_2 : dependence to the temperature of the heat loss coefficient (Wm⁻²K⁻²)

c_5 : effective thermal capacity (Jm⁻²K⁻¹)

F : focus distance (m)

F' : heat removal factor also called thermal efficiency (-)

G_{DNI} : direct normal irradiance (Wm⁻²)

G_T : global irradiance on collector plane (Wm⁻²)

G_{dT} : diffuse irradiance on collector plane (Wm⁻²)

- 49 G_{bT} : direct irradiance incident on collector plane = $G_{DNI} \times \cos \theta_i$ (Wm^{-2})
- 50 K_b : incidence angle modifier relative to the direct incidence radiation (-)
- 51 K_d : incidence angle modifier relative to the diffuse radiation (-)
- 52 k : extinction coefficient (m^{-1})
- 53 N : total number of mirrors
- 54 \dot{Q} : output power (W)
- 55 t : time (s)
- 56 t_a : ambient temperature ($^{\circ}\text{C}$)
- 57 t_e : output fluid temperature ($^{\circ}\text{C}$)
- 58 t_{in} : inner fluid temperature ($^{\circ}\text{C}$)
- 59 t_m : average fluid temperature $t_m = (t_e + t_{in})/2$ ($^{\circ}\text{C}$)
- 60 W : aperture width
- 61 y : fitting dependent variable
- 62 z_i : fitting independent variable

63

64

65 **Abbreviation**

- 66 CPC: Compound Parabolic Collector
- 67 CSFMSC: Curved Slats Fixed Mirror Solar Concentrator
- 68 CCStaR: Concentrating Collector with Stationary Reflector
- 69 ETC: Evacuated Tube Collector
- 70 FMSC Fixed Mirror Solar Concentrator
- 71 FPC: Flat Plate Collector
- 72 IAM: Incidence Angle Modifier
- 73 ISO: International Organization for Standardization
- 74 LFR: Linear Fresnel Reflector
- 75 MAE: mean absolute error
- 76 ME: mean error
- 77 MLR: multiple linear regression
- 78 PTC: Parabolic Trough Collector
- 79 RMSE: root mean square error
- 80 SRТА: Stationary Reflector with Tracking Absorber
- 81 WLS: Weighted Least Square

1. Introduction

Solar thermal concentrator devices focus sunlight into a receiver in order to obtain elevated efficiencies at high temperatures. In some cases, the geometry of these devices is modified in function of the position of the sun. For example, in the Linear Fresnel Reflector (LFR) [1] the mirrors are moved to redirect the sun rays into a fixed linear receiver; and in the case of the Fixed Mirror Solar Concentrator (FMSC) [2], or the Stationary Reflector with Tracking Absorber (SRTA) [3], the receiver moves within a circular path while the reflector remains static. Another typical example is the configuration of a central tower plant [4], where the reflectors (heliostats) are moved to reflect the sun rays towards a central point receiver. All these optical systems are examples of a variable geometry concentrator, and differ from the designs of the Parabolic Trough Collector (PTC), and parabolic dishes, where the relative position between the mirror and the receiver does not change during the day (the geometry remains constant).

New types of collectors in the medium temperature range (80-250°C) [5] have emerged lately, such as the LFR from PSE AG [6] and the fixed-mirror CCStaR prototype (Concentrating Collector with Stationary Reflector) [7]. These solar concentrators are systems with variable geometry, and a testing procedure is needed in order to certify their behaviour in real working conditions; as is the case for the ISO standards used to certified conventional collectors for domestic hot water or space heating, i.e. Flat Plate Collectors (FPC), Evacuated Tube Collectors (ETC), and Compound Parabolic Collector (CPC).

There are standards that provide the testing procedure for the thermal performance of solar systems. The withdrawn European norm EN 12975-2 [8] and the new version of the International Standard ISO 9806:2013 [9] that replaced the European Standard [8] are applicable to the most typical collectors available in the market (FPC, ETC, and CPC), where the quasi-dynamic thermal performance of glazed and unglazed liquid heating solar collectors is specified. Tracking concentrating collectors were more detailed in those standards [8, 9] because of the separation between direct and diffuse efficiency gives a more accurate characterization of a tracking concentrating collector. Unfortunately, the standards cannot be applied to concentrators with complex Incidence Angle Modifiers (IAM), as is the case for variable geometry collectors, because they do not specify the procedure for experimentally determining the IAM when it is not feasible to obtain all the measuring angles. The American Standard ASTM 905 [10] applies the quasi-steady state conditions to a one- or a two-axis tracking reflecting concentrating collector. This testing method can be applied to collectors with a geometric concentration ratio of seven or greater, as the effects of diffuse irradiance on performance are negligible. However, this testing method is not intended for, and may not be applicable to fixed-mirror tracking-receiver collectors. On the other hand, the American Standard ASHRAE 93 [11] can be applied to a solar concentrator, even though only direct radiation is used for the steady-state model, and not much detail to particular testing processes for solar concentrators with variable geometry is mentioned.

In many studies, the thermal testing procedures stipulated in the standards have been applied to a solar concentrator. Jaramillo et al [12] tested a PTC according to the ASHRAE 93 [11], as well as Nkwetta and Smyth [13] did for a low-concentrator

evacuated system. Xu et al [14] realized a comparison of three outdoor test methods for determining the thermal performance of PTC's: the steady-state method of the ASHRAE 93 [11], the quasi-dynamic method of the EN 12975-2 [8], and a new dynamic method developed by the authors. In addition, solar concentrators can be thermally characterized by energy balance equations, and as a result, there are many studies that have not implemented the standards but have instead applied their own models, with examples being, the latter study mentioned above [14], or the experimental validation for a LFR prototype by Pino et al [15], or the newly proposed models to characterize solar thermal collectors [16, 17].

The authors of this paper had tested in [18] a solar concentrator prototype with variable geometry called CCStaR V2 (a prototype similar to the one analysed in this paper called CCStaR V1). A new procedure to characterize the prototype optically and thermally, based on the quasi-dynamic model of the standard EN 12975-2 [8], was presented, which “dummy variables” method [19] and the optical results of a ray-tracing simulation used as initial hypothesis for the energy balance equation were the main contributions. The study showed some deficiencies in the EN 12975-2 standard for variable geometry concentrators such as: the lack of definition for the requirements of the IAM in the testing procedure, the lack of the thermal efficiency procedure if the efficiency at normal incidence could not be acquired from testing due to the characteristics of the solar concentrator (collectors with large structures and with cumbersome orientation adjustments), and difficulties in obtaining the effective thermal capacity term for solar thermal concentrators. We proposed in [18] the use of ray-tracing software in order to assess the initial hypotheses for the collector thermal model,

stipulating the condition that the simulation results must fall within a $\pm 5\%$ error from the experimental results. In this procedure, it was also found necessary to add the heat removal factor F' obtained from previous testing.

Therefore, if solar concentrators with variable geometry must be certified, experimentation with these systems would be of great value to propose new changes in the future standards revisions.

The solar concentrator prototype tested in this paper, the CCStaR V1, is made up of a fixed parabolic mirror with a moving receiver that tracks the sun in a circular path. Although a parabola only has one focus point for normal incidence, given a high enough F/W ratio (where F is the focus distance and W the aperture width), the radiation dispersion can be confined to a reduced area for all significant sun angles (from the energy point of view). Furthermore, the radiation concentration area falls in a circular path which can be easily tracked with the rotating arm of the tube receiver shown in Figs. 1(a) and (b). The receiver angle position θ_r is the angle between the axis that links the receiver to its rotational axis and that of the parabola, see θ_r in Fig. 2(b). The receiver is positioned at an angle $\theta_r = 2\theta_T$, where θ_T is the incidence angle on the reflector in the transversal plane.

In this paper, a new methodology is proposed to characterize the thermal efficiency curve of a variable geometry collector, where the obtained IAM results from a ray-tracing program are introduced as the known independent variables in the energy balance equation. The main differences with respect to the previous studies are: “dummy variables” were not used, the experimental measurement of the thermal

efficiency at normal incidence was not required, and the heat removal factor F' was obtained from the test.

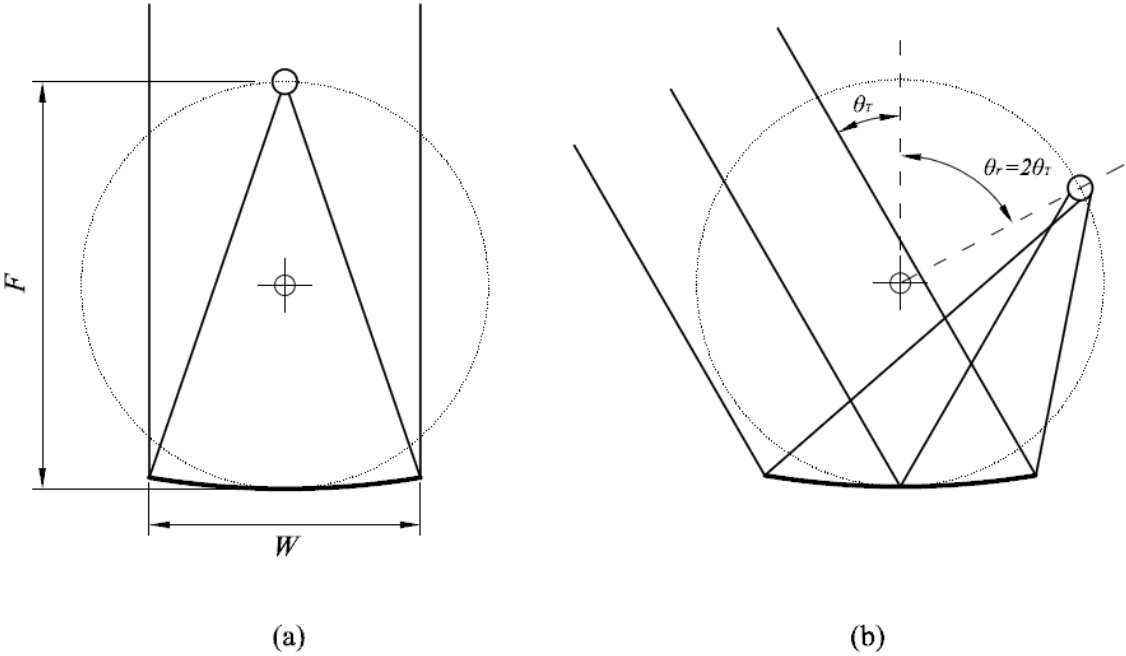


Fig. 1. (a) A parabola with a high F/W ratio focusing sun rays on a receiver for normal incidence, and (b) the same parabola focusing sun rays on a receiver for $\theta_T=30^\circ$ incidence angle.

Reproduced in [18]. Copyright 2014 by Elsevier.

2. The solar concentrator with variable geometry

From an optical point of view, a great difference exists between fixed geometry and variable geometry collectors, as the former type usually has a simple model for the IAM (i.e. the Souka and Safwat IAM model [20] which is used in many standards, i.e. [8, 9, 11]), while variable geometry concentrators usually have a complex IAM that is not

easily predictable [18, 21]. On account of this, standards must explain in detail the procedure used to obtain the IAM values for all transverse and longitudinal angles.

2.1 Related work

The company Tecnología Solar Concentradora SL (www.tsc-concentra.com), in collaboration with the University of the Balearic Islands (UIB), has developed a solar concentrator with fixed mirror and tracking absorber called CCStaR. The CCStaR project started in 2006 with the aim of bringing to the market a solar collector able to work between 100 and 200°C that could at the same time be easily integrated onto light building roofs. The CCStaR optical principles were based on the Fixed Mirror Solar Concentrator (FMSC) geometry [2]. The FMSC emerged in the seventies as an effort to reduce the electricity production costs of solar thermal power plants [22]. The FMSC concept was the starting point for the CCStaR project (see [23] for more details about this geometry).

While the original idea for the CCStaR project was to develop a solar concentrator based on the FMSC, it was demonstrated that replacing the flat mirrors with curved ones resulted in a better optical performance [24, 25]. The design with curved mirrors has been named the Curved Slats Fixed Mirror Solar Concentrator (CSFMSC). In a previous study [26], an optical analysis using ray-tracing tools was made in function of three design parameters: the number of curved mirrors N , the ratio of focal length and reflector width F/W , and the aperture concentration C_a (defined as the ratio of the mirror aperture/absorber aperture). Further studies on the thermal behaviour of both geometries

(FMSC, CSFMSC) have been presented recently [27, 28], and comparing the results of both geometries, it was shown that the CSFMSC, with only one parabolic mirror, is the design with a higher solar energy capture.

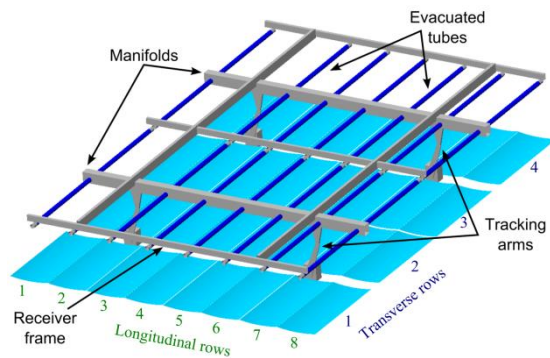
During the CCStaR project, three prototypes were constructed and evaluated. The first one was based on the FMSC geometry with nine flat mirrors ($N=9$) and a ratio $F/W=1.5$, while the other two were based on the CSFMSC geometry with one parabolic mirror ($N=1$), and a ratio $F/W=1.5$ for the second prototype and a ratio $F/W=1.1$ for the third. The testing results of the first prototype (called CCStaR V0) have been presented in [21], where a ray-tracing program developed by the authors (described in [23]) was used in order to determine the optical behaviour of the system, and the results showed great agreement between the simulated and tested results (the CCStaR V0 prototype was tested only at ambient temperature). A complex IAM was observed for this first prototype, where the transverse IAM curve was not an easy fit. For the third prototype (CCStaR V2), an optical and thermal characterization was presented in [18]. The same ray-tracing program [23] was used to set the initial hypothesis for the optical terms of the energy balance equation proposed in the standards [8, 9], and “dummy variables” where used due to the complexity of the IAM. During the CCStaR V2 testing campaign, the normal incidence was obtained experimentally, as it is mandatorily specified in the standards [8, 9]. It should be noted that it was only possible to measure the thermal behaviour at a normal incidence near the time of summer solstice, because the CCStaR V2 cannot be reoriented to the sun easily without an expensive rotating test platform due to the large mirror dimensions (a fixed mirror with gross area of 43.7 m^2).

In this paper, a new methodology to characterize variable geometry collectors is presented that has been applied to the second CCStaR prototype that was constructed (the CCStaR V1). The methodology consists of first validating a theoretical ray-tracing model with experimental results at near ambient temperature, and in which the heat removal factor F' is obtained in this first step. Once the theoretical ray-tracing model was validated, it was then used to calculate the optical efficiency for each sun position during the testing campaign in order to introduce the IAM values in the energy balance equation as known independent variables. Therefore, “dummy variables” were not used, and therefore it was unnecessary to measure the thermal efficiency at normal incidence. Finally the heat loss coefficients are determined from data series at average working temperatures greater than the ambient. The results showed that the ray-tracing tools proved to be very helpful to extend the scope of the standards.

2.2 Description of the CCStaR V1 prototype

The tested prototype is the CCStaR V1 (Concentrating Collector with Stationary Reflector Version 1), and it was manufactured with the following design parameters: $F/W=1.5$, $N=1$, and $C_a=11.5$. The optical principle of the CCStaR V1 is the same as the one of the CCStaR V2 and it is shown in Fig. 1 (see [18] for more details about the tracking receiver path). The construction of the V1 prototype is very similar to the V2, as the only main differences are element size, and that the V1 prototype is smaller than the V2 version (23.7 m^2 and 37.4 m^2 of aperture area respectively).

The Figure 2(a) is a drawing of the prototype. The gross dimensions are 4.5 m in width by 6 m long. The reflector consists of 32 parabolic mirrors distributed in eight longitudinal and four transverse rows. The receiver consists of 32 standard Sydney evacuated tubes also mounted in eight longitudinal and four transverse rows, and positioned on a mobile structure that tracks the sun trajectory on a circular path in order to optimize the focusing point onto the receiver. Two manifolds distribute the working fluid into the receivers. The reflector was made of aluminium sheets for solar applications. The width of each parabola was 540.5 mm, and the total aperture area (reflector surface) was 23.7 m^2 . The absorber surface was the inner cylindrical glass of a Sydney tube (47 mm diameter), while the outer glass tube was 58 mm in diameter. The CCStaR V1 was located on the rooftop of a building at the UIB in Mallorca, (latitude $39^\circ 38' 15''$, longitude $2^\circ 38' 47'' \text{E}$, and altitude 84 m) with a tilt angle of 15° and was oriented 9° East; see Fig. 2(b) for an entire visualization of the CCStaR V1 prototype.



(a)



(b)

Fig. 2. (a) 3D image of the CCStaR V1 showing the main elements, and (b) picture of the CCStaR V1 installed at the UIB in Mallorca.

3. Testing methodology

In order to test the CCStaR's V1 and V2 prototypes under quasi-dynamic conditions, a test bench was constructed and was given as described in [18]. The only difference respect to the CCStaR V2 test bench is that a 12 kW cooler was introduced between the collector outer fluid and the air heater in order to measure the thermal efficiency at ambient temperature. Measurements of the sensors were recorded every five seconds, and the measurement uncertainty estimation was presented in the previous article (see [18] for more details about the bench testing).

The testing methodology used for the CCStaR V1 prototype was the quasi-dynamic model that is explained in detail in section 25.1.4 of the International Standard ISO 9806 [9]. The Eq. (1) shows a slightly modified version of the model presented in this standard:

$$\frac{\dot{Q}}{A_a} = F' \eta_{0b}^{opt} K_b G_{bT} + F' \eta_{0d}^{opt} K_d G_{dT} - c_1 (t_m - t_a) - c_2 (t_m - t_a)^2 - c_5 \frac{dt_m}{dt} \quad (1)$$

The F' is the heat removal factor, the η_{0b}^{opt} and η_{0d}^{opt} are the optical efficiency at normal incidence relative to the beam and diffuse solar irradiation respectively (only optical effects), the K_b and K_d are the IAM for the beam and diffuse solar irradiation respectively, and the t_a is the ambient temperature. The variables G_{bT} and G_{dT} are the beam and diffuse solar irradiance, respectively, (both on the collector plane referred to with the T sub-index). The coefficients c_1 and c_2 are the heat loss coefficients referred to the difference between average fluid temperature t_m and the ambient temperature t_a . The

coefficient c_5 is the effective thermal capacity which depends on the derivate in time of the mean fluid temperature dt_m/dt .

The coefficients related to the thermal losses due to the effects of wind speed (c_3 and c_6 in the standards [8, 9]) were ignored because the selected testing days were all classified as “low wind speed” (wind speed lower than 2 m/s). Likewise, the coefficient related to the long-wave thermal losses (c_4 in the standards [8, 9]) was also omitted because the effects of irradiation are reduced by the glass tube.

The IAM terms are calculated by the ratio between the optical efficiency for any sun position and the optical efficiency at normal incidence:

$$K_b = \frac{\eta_b^{opt}(\theta_T, \theta_L)}{\eta_{0b}^{opt}} \quad (2)$$

$$K_d = \frac{\eta_d^{opt}(\theta_T, \theta_L)}{\eta_{0d}^{opt}} \quad (3)$$

where θ_T and θ_L are the transverse and longitudinal angles (for a definition of those angles see for example [18, 29]).

For the FMSC and CSFMSC theoretical designs in [23, 26], it was shown that beam IAM can be factorized in a similar way to the CPC collectors by the product of the transverse and longitudinal IAM, $K_b(\theta_T, \theta_L) = K_b(\theta_T, 0)K_b(0, \theta_L)f(\theta_T, \theta_L)$, where $f(\theta_T, \theta_L)$ is a function that takes into account the longitudinal end losses.

Normally, the treatment of Eq. (1) is solved by Multiple Linear Regression (MLR) in order to obtain the constant parameters. The measure of thermal efficiency at zero thermal losses and normal incidence is mandatory in the standards [8, 9], so the values

306 $F'\eta_{0b}^{opt}$ and $F'\eta_{0d}^{opt}$ must be obtained experimentally. For bi-axial systems, the IAM
 307 depends on the transverse and longitudinal angles, hence the ISO 9806 mandates that
 308 the IAM curve be obtained for both principal planes and selected angles (20°, 40°, 60°
 309 ...), and this can usually be done with mobile platforms for small-size collectors.

310 For the case of the CCstaR V1 and V2 prototypes, the usual method described above is
 311 not applicable because of the large dimensions of the prototype do not allow
 312 reorienting. Therefore only IAM values at the sun incidence angles available during the
 313 testing campaign can be obtained. In Sallaberry et al. [18], the thermal behaviour at
 314 normal incidence was measured because the sun trajectory allowed it. However, this
 315 implies that the experimental campaign can only be performed when the sun passes
 316 through the zenith of the collector. Therefore, another methodology is required to obtain
 317 the constant parameters in Eq. (1) if, due to the collector configuration, the sun does not
 318 pass through the zenith of the collector. Moreover, this new methodology can be useful
 319 for in situ measurements.

320 The new methodology described here, which combines ray-tracing results with thermal
 321 and climatic measurements, enables the c 's coefficients to be obtained without
 322 measuring the $F'\eta_{0b}^{opt}$ and $F'\eta_{0d}^{opt}$ values. The proposed method consists of rewriting
 323 Eq. (1) when the collector is working at average temperature near to the ambient
 324 temperature as:

$$325 \quad \frac{\dot{Q}}{A_a} = F' \{ \eta_{0b}^{opt} K_b G_{bT} + \eta_{0d}^{opt} K_d G_{dT} \} - c_5 \frac{dt_m}{dt} \quad (4)$$

326 We call Eq. (4) the optical model. For the optical model, the curve to fit is:

$$y = b_1 z_1 + b_2 z_2 \quad (5)$$

where $y = \frac{\dot{Q}}{A_a}$ is the dependent variable, and z_i are the independent variables defined as:

$$z_1 = \eta_{0b}^{opt} K_b G_{bT} + \eta_{0d}^{opt} K_d G_{dT} \quad (6)$$

$$z_2 = \frac{dt_m}{dt} \quad (7)$$

Hence the parameters to determine in the fitting are related to the parameters:

$$b_1 = F' \quad (8)$$

$$b_2 = -c_5 \quad (9)$$

Here the heat removal factor F' is obtained by fitting the compared ray-tracing results and experimental data at ambient temperature, because the optical terms $K_b \eta_{0b}^{opt}$ and $K_d \eta_{0d}^{opt}$ were determined previously by ray-tracing simulation for each sun position during the testing campaign. Note that the optical terms ($K_b \eta_{0b}^{opt}$ and $K_d \eta_{0d}^{opt}$) are considered as independent variables in the model, hence the problem of not having a clear IAM model is avoided.

Once the optical model is validated (it means that Eq. (4) reproduces the experimental results within ± 5 % difference) the thermal model (Eq.(1)) is used to obtain the heat loss coefficients by using data series with average working temperatures greater than the ambient.

The uncertainty of each characteristic parameter has been calculated according to the method published in the ISO 9806 [9] and the International Standard [30]. The uncertainties of the sensors were described in [18].

In order to validate the integrity of the thermal model (Eq. (1)) with respect to the experimental values, three error estimators were used: the mean error ME, the mean absolute error MAE, and the root mean square error RMSE. Equations (10-12) show the expressions for each error estimator:

$$ME = \frac{1}{N} \sum_{i=1}^N \frac{\dot{Q}_{exp} - \dot{Q}_{mod}}{\dot{Q}_{exp}} \quad (10)$$

$$MAE = \frac{1}{N} \sum_{i=1}^N \left| \frac{\dot{Q}_{exp} - \dot{Q}_{mod}}{\dot{Q}_{exp}} \right| \quad (11)$$

$$ME = \frac{1}{N} \left[\sum_{i=1}^N \left(\frac{\dot{Q}_{exp} - \dot{Q}_{mod}}{\dot{Q}_{exp}} \right)^2 \right]^{1/2} \quad (12)$$

4 Ray-tracing simulations

A forward ray-tracing code was implemented and described in [23], with an update adding diffuse radiation simulation given in [18]. In the ray-tracing program, the geometry of the solar concentrator can be composed by static and mobile surfaces. The mobile surfaces change their location depending on the sun location, which it is very useful to analyse variable geometry concentrators optically. The optical efficiencies (beam and diffuse) have been calculated with this program, but first a simple geometric

characterization was conducted to determine the real position of each evacuated tube respect to its parabolic mirror.

4.1 Geometrical characterization

The position of both edges of each tube was measured with a laser meter and a caliper to find the relative position between each receiver tube and its corresponding parabolic mirror. It was possible to measure deviations within ± 1 mm tolerance between the theoretical and the real position. In Fig. 3 the deviation in vertical and transverse position from the theoretical position is shown, and in Tables 1 and 2 the values of the relative positioning error are shown for each receiver tube. It can be observed that the errors in the transverse direction (Table 1) were not greater than 4 mm. This positioning error, despite being very small compared to the overall dimensions of the device, could cause significant losses for sun angles corresponding to low solar elevation. However, it should be noted that only two tubes were positioned with an error > 2 mm. With regard to errors in the vertical direction (Table 2), the tubes in the central part were quite well positioned. However, at the edges, where the deformation of the support structure was greater, the errors were rather large, and reached values up to 18 mm. Nevertheless, it was observed that 14 tubes were positioned with a vertical error of ≤ 2 mm.

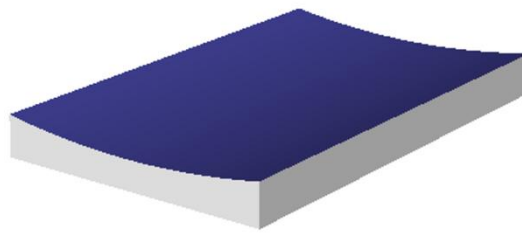
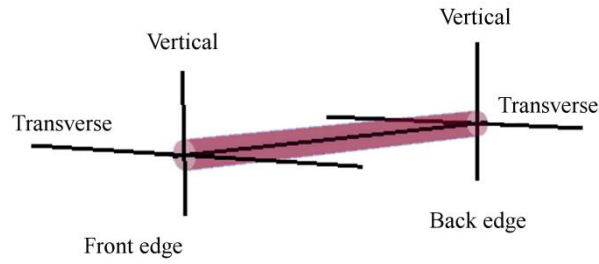


Fig. 3. Deviation in relative positioning, transverse and vertical directions, between the receiver tube and the parabolic mirror

Table 1. Relative positioning errors between reflectors and receiver tubes in the transverse direction.

Transverse relative positioning errors (mm)			Longitudinal row							
			1	2	3	4	5	6	7	8
Transverse row	1	front edge	-1	0	1	0	-1	2	2	0
		back edge	-1	-1	0	0	0	0	-1	-1
	2	front edge	0	1	0	0	-1	-1	1	2
		back edge	1	1	1	1	3	2	4	2
	3	front edge	0	1	0	1	1	1	0	1
		back edge	1	1	1	1	2	1	0	0
	4	front edge	0	1	-1	0	0	0	2	2
		back edge	0	0	-2	1	-1	1	2	-1

Table 2. Relative positioning errors between reflectors and receiver tubes in the vertical direction.

Longitudinal relative positioning errors (mm)			Longitudinal row							
Transverse row			1	2	3	4	5	6	7	8
	1	front edge	-1	-4	-5	-6	-8	-10	-11	-12
		back edge	2	-2	-3	-1	-1	-1	0	0
	2	front edge	1	1	1	1	2	1	5	3
		back edge	-1	-1	0	0	2	2	3	0
	3	front edge	0	-1	0	2	1	2	2	2
		back edge	2	2	1	1	1	0	0	3
	4	front edge	0	-2	-3	-3	-2	-3	-2	-4
		back edge	-8	-10	-13	-14	-14	-15	-15	-18

4.2 Ray-tracing results

In this Subsection the IAM curves are presented. Figure 4 shows a visualization of the ray-tracing for the CCStaR V1 for solar beam irradiation simulation. The geometry of the CCStaR V1 was modelled with the material physical properties of the prototype as reported by the manufacturers (see Table 3), and with the position errors displayed above.

A convergence analysis was conducted before each numerical experiment in order to determine the minimum number of rays needed to be computed in the ray-tracing to obtain a result variability of less than 0.004. Nevertheless, the biggest contribution to the results is due to the errors associated to the input optical parameters, such as: the cover transmittance, receiver absorptance, and the mirror reflectance. A sensitivity study was conducted to assess the influence of the optical parameters on the ray-tracing results. We only considered errors for the normal incidence absorptance ($\alpha_0=0.94\pm0.01$), extinction coefficient ($k=8\pm2 \text{ m}^{-1}$), and mirror reflectance layer ($\rho=0.91\pm0.01$). Taking

into consideration the upper and the lower limit errors exposed above, the ray-tracing results varied by ± 0.03 when the CCStaR V1 was simulated by the normal beam irradiation and diffuse irradiation. Therefore, we considered an accuracy of ± 0.03 for the ray-tracing results to be a consequence of the input parameters.

A total optical error was included for the mirror imperfections by considering a Gaussian distribution with a variance value of $\sigma = 10$ mrad, which includes the whole dispersion caused by the following sources errors: slope, scattering, tracking, and alignment [31]. The size of the sun was modelled by the Buie equations [32] with a circumsolar ratio of 0.05.

Taking all of these considerations into account, by issuing 10^6 rays at normal incidence, beam optical efficiency was determined to be $\eta_{ob}^{opt} = 0.70 \pm 0.03$.

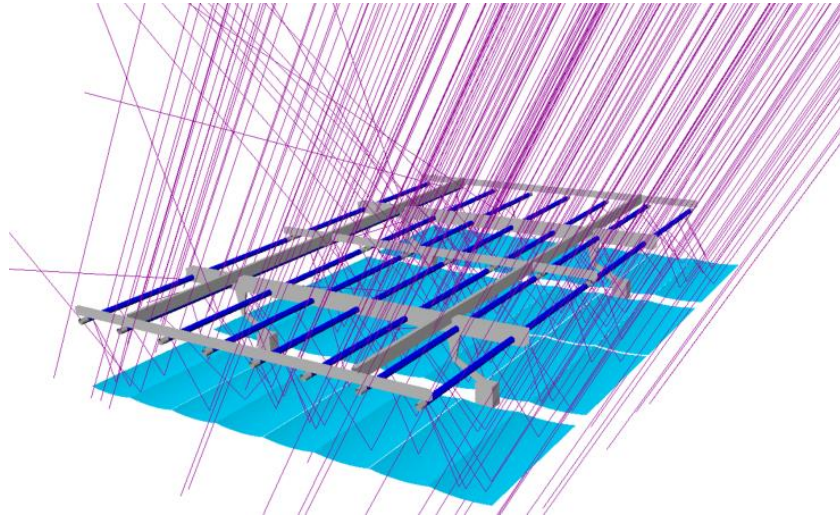


Fig. 4. Optical simulation by ray-tracing program for beam solar irradiation.

415 **Table 3. Optical properties of the materials.**

Element	Property
Mirror solar reflectance	$\rho = 0.91$
Standard deviation combining all optical errors	$\sigma = 10 \text{ mrad}$
Glass tube refraction coefficient	1.526
Glass tube extinction coefficient	8 m^{-1}
Solar absorptance at normal incidence	$\alpha_0 = 0.94$
Angular absorptance dependence (adopted from [33])	$\frac{\alpha}{\alpha_0} = 1 - 0.057 \left(\frac{1}{\cos \theta_i} \right)^{1.2}$

416

417 Figure 5(a) shows the results for the beam transverse and longitudinal IAM. It can be
418 observed that the transverse IAM was greater than 0.8 for incidence angles up to 54°.
419 An abrupt decrease occurred for an incidence angle of 60°, which is the transverse angle
420 for which the tracking movement was stopped due to a mechanical intersection in the
421 support structure of the prototype. The longitudinal IAM drops rapidly when the
422 incidence angle increases; this was due to very high edge losses (there was a lack of
423 reflective surface in the longitudinal direction between transverse beams, and also a lack
424 of absorber surface in the longitudinal direction between the manifolds).

425 The beam IAM for all combinations of the transverse and longitudinal angles was
426 determined by ray-tracing and the results have been plotted in Fig. 5(b) (grey surface).
427 The factorized approximation for the beam IAM was also plotted, and was calculated
428 according to the expression $K_b(\theta_T, \theta_L) = K_b(\theta_T, 0)K_b(0, \theta_L)f(\theta_T, \theta_L)$, black points in Fig. 5(b),
429 in order to compare this approximation given in [26] with the exact value obtained by
430 ray-tracing simulation. The Pearson correlation between the IAM factorization and the
431 ray-tracing results was $r=0.966$. Thus, the beam IAM factorized approximation was
432 valid for this prototype, as it has been proven for theoretical CSFMSC designs in [26].

It should be noted that the optical behaviour of the prototype was very irregular and not easily predictable by analytical methods, and as a result could only be calculated accurately with computer ray-tracing tools. Moreover, if the transverse and longitudinal IAM curves are given, and the beam IAM factorized approximation is validated, the beam optical behaviour of the CCStaR V1 can be obtained similarly to the bi-axial collectors by factorization.

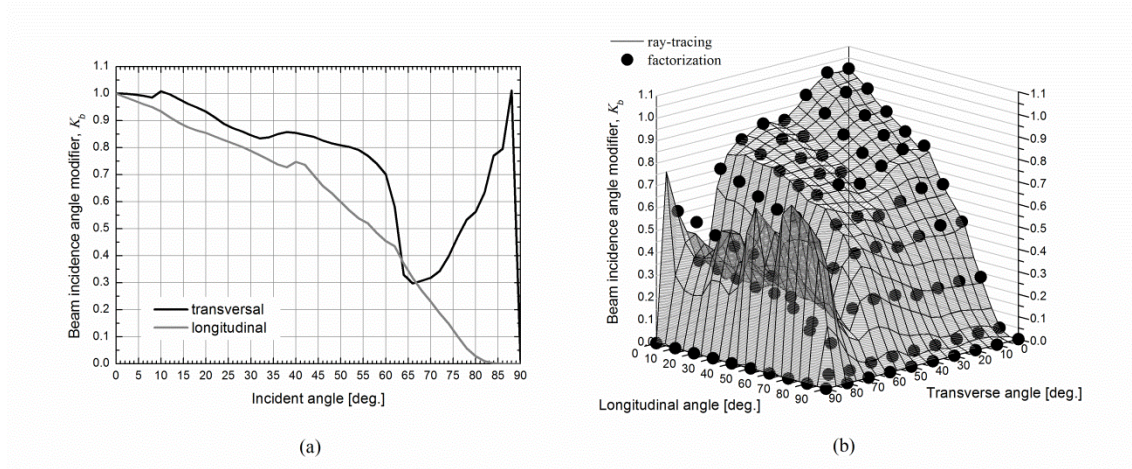


Fig. 5. IAM curves for CCStaR V1 collector calculated with ray-tracing program: (a) transverse and longitudinal IAM and (b) IAM values of the CCStaR V1 collector for overall angular range.

Given that the receiver is mobile, the optical efficiency for diffuse solar irradiation could depend on the position of the receiver, something which is not the case for a fixed geometry collector. A simulation by ray-tracing was performed to calculate the diffuse solar irradiation efficiency for different receiver positions, because the receiver angle position θ_r depends only on the transverse angle as it was explained in [18] (see Fig. 1). In this case, the ray-tracing results were determined by issuing 10×10^6 rays for each receiver position. The results are presented in Fig. 6 for a tilt inclination of 15° . The maximum value was obtained when the receiver was positioned at the highest location

on the path circle, $\eta_{od}^{opt}(\theta_T = 0^\circ) = 0.154$, and the minimum value was obtained when $\theta_T = 20^\circ$, $\eta_d^{opt}(\theta_T = 20^\circ) = 0.133$. Fig. 6 shows that the receiver position had a slight influence on the optical efficiency for diffuse solar irradiation, hence an average between $\theta_T = 0^\circ - 90^\circ$ is a good approximation, which gives a value $\eta_{od}^{opt} = 0.14 \pm 0.03$ (the error was due to the input parameters in the ray-tracing). With this approximation, the IAM for diffuse irradiation is always $K_d = 1$.

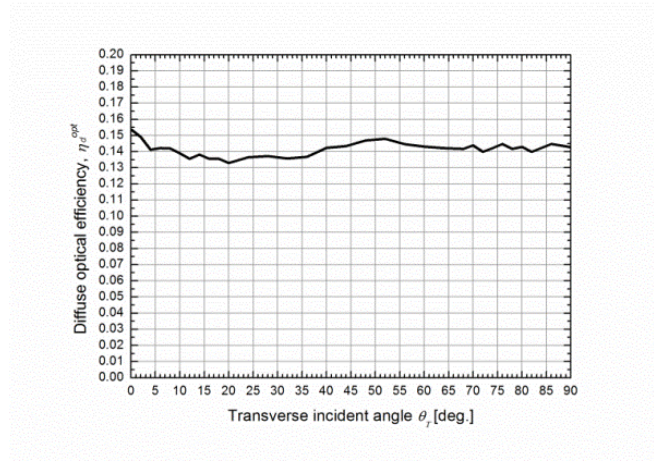


Fig. 6. Diffuse optical efficiency $\eta_d^{opt}(\theta_T)$ obtained by ray-tracing simulation.

5 Experimental results and discussion

The prototype was tested at average working temperature t_m from the ambient temperature up to 118°C . The tests at ambient temperature were used to determine the collector heat removal factor F' , and to validate the ray-tracing simulations (the optical model explained in Eq. (4)). Tests were performed at an average working temperature

greater than the ambient temperature to determine the heat loss coefficients in the energy balance equation (Eq. (1)).

In order to avoid any noise during the data processing, the requirements presented in Table 4 were used as data quality control. A preconditioning time of ten minutes was used where the data were to be checked but not to be used in the fitting. The tests were performed over 10 days, and 93 points were obtained (45 were at average working temperature near to the ambient, $t_m = t_a \pm 5 \text{ K}$, and 48 data points at higher temperature, range of 65°C to 118°C).

Table 4. Requirements to obtain reliable points from experimental measurements.

Sensor data	Specification
Preconditioning time	600 seconds
Time for each stable point	300 seconds
Deviation in the inlet temperature for each stable point	$\pm 1 \text{ K}$
Deviation in the volumetric flow for each stable point	$\pm 1 \%$
Beam solar irradiation for each stable point	$G_{bT} > 400 \text{ W/m}^2$
Deviation in flow during the testing campaign	$\pm 15 \%$

In Figure 7(a) the $t_m - t_a$ values versus global solar irradiance on the mirror aperture G_T are shown for the stable experimental points. Most of the data were collected during sunny days with a G_{dT}/G_T ratio between 0.14 and 0.31, see Fig. 7(b). Stable points could only be measured in areas away from normal incidence because some ruptures of the Sydney tubes were detected at high irradiation concentrations (for more details about this cracking see [34]). Figure 8 shows the transverse and longitudinal angles obtained during the testing. It should also be noted that the transverse and longitudinal

angles tested in this experiment fall within the range of the most important sun angles for this geometry and location, as it was shown in [35].

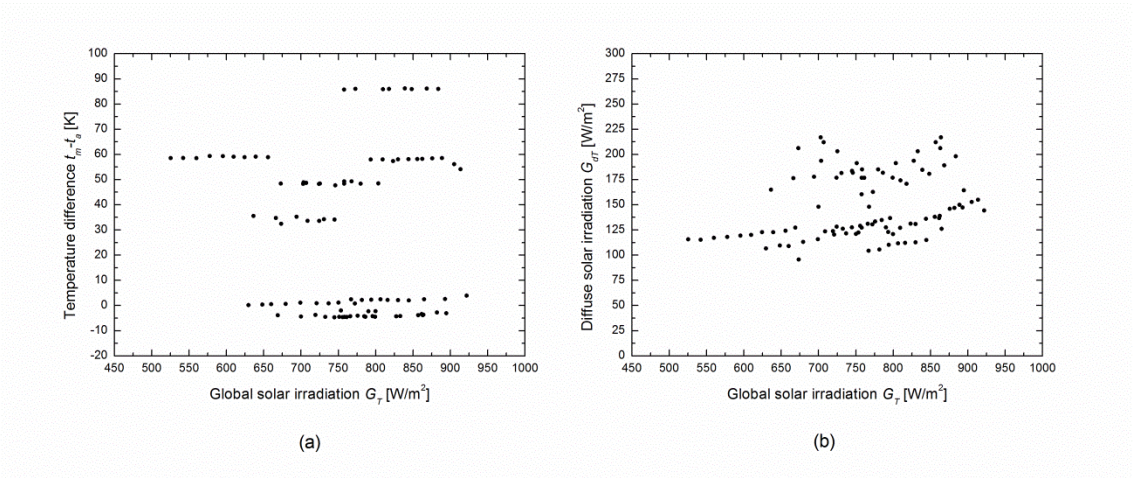


Fig. 7. Variability of the data: (a) temperature difference $t_m - t_a$ vs global irradiance G_T , and (b) diffuse irradiance G_{DT} vs global irradiance G_T .

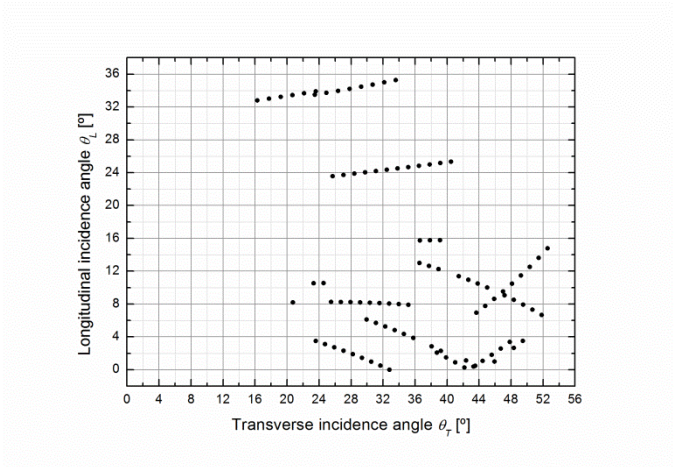


Fig. 8. Incidence angles during the testing.

5.1 Ray-tracing validation and F' value determination

The prototype was tested at ambient working temperature ($t_m \approx t_a \pm 5$ K) in order to find the F' value and to validate the ray-tracing simulations. The WLS method exposed in [9, 30] was performed to obtain the b_1 and b_2 parameters given in Eqs. (5-9). The results of the WLS are shown in Table 5, where the value of the heat removal factor obtained was $F'=0.934\pm0.009$.

For the goodness of fit in the adjustment regression, the t-ratio is defined as the value/uncertainty coefficient used. The t-ratio must be greater than two in order to be accepted into the efficiency curve [8, 36], even though the new version of the International Standard ISO 9806:2013 [9] states that the t-ratio must be greater than three. We can observe that the F' value was obtained with a low uncertainty with a t-ratio of 106, which is not the case of the capacity term c_5 with a t-ratio of 2.6.

Figure 9 shows the optical model Eq. (4) versus the experimental output power for the 45 stable points at ambient temperature. There was a good agreement between the experimental and the theoretical values, as all the points fell within the $\pm 5\%$ error, as can be seen in Fig. 9. Hence, the optical model has been validated in view of the results and we determined that the beam efficiency at normal incidence was $F'\eta_{0b}^{opt} = 0.66 \pm 0.03$, and the diffuse efficiency was $F'\eta_{0d}^{opt} = 0.13 \pm 0.03$.

Table 5. Parameters identified from fitting the optical model Eq.(4).

Parameter	Unity	Value	Uncertainty	t-ratio
F'	-	0.934	0.009	106
c_5	Jm ⁻² K ⁻¹	-12647	4824	2.6

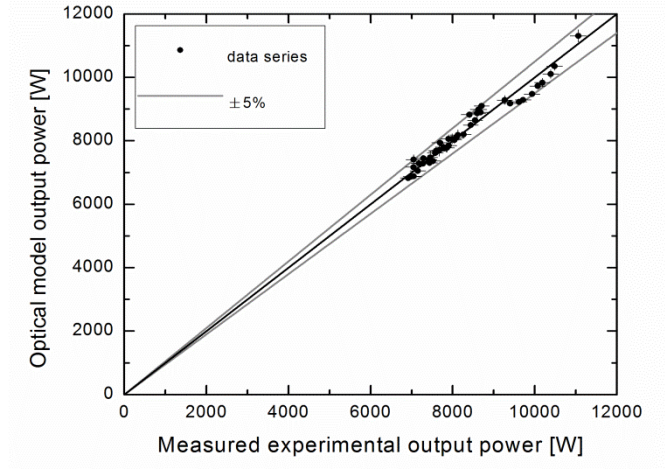


Fig. 9. Experimental output power at ambient working temperature versus optical model power.

5.2 Thermal power curve fitting

Once the optical model was validated, the 48 stable points at average working temperature greater than the ambient temperature were used to determine the thermal loss coefficients. The proposed model was the one given in Eq. (1) where the $F'\eta_{0b}^{opt}$ and $F'\eta_{0d}^{opt}$ values from the previous analysis were used. Note that the beam IAM values (K_b) were required for the adjustment and obtained previously by ray-tracing simulation for each sun position in the tests. Hence, the proposed power curve was the one shown in Eq. (13), and has been called as Model 1.

$$\frac{\dot{Q}}{A_a} = 0.66 \times K_b G_{bT} + 0.13 \times G_{dT} - c_1(t_m - t_a) - c_2(t_m - t_a)^2 - c_5 \frac{dT_m}{dt} \quad (13)$$

Again, the WLS method exposed in [9, 30] was performed in order to obtain the c 's coefficients. The capacity term c_5 was added in the thermal model due to the high

uncertainty obtained in the previous optical model. The results are given in Table 6, and it can be observed that the first thermal loss coefficient obtained a t-ratio lower than 2. Hence, a second model (Model 2) was proposed, only taking into consideration the second term for thermal losses, due to the high uncertainty on the c_1 parameter, Eq. (14):

$$\frac{\dot{Q}}{A_a} = 0.66 \times K_b G_{bT} + 0.13 \times G_{dT} - c_2 (t_m - t_a)^2 - c_5 \frac{dT_m}{dt} \quad (14)$$

In Table 6 the results of the Model 2 are also shown, and it can be observed that the c_2 parameter was obtained with a t-ratio greater than 17, which is higher than the one obtained in the first model with a t-ratio of 2.91.

For the c_5 parameter, as was presented in [18], a high relative uncertainty was obtained. This was because it is not possible to obtain enough variability in time for the average temperature t_m , due to the fact that cloudy days were not contemplated during the testing campaign because they do not provide representative data in a solar concentrator. Either way, the values obtained for the c_5 in the three adjustments belong to the ranges limited by the uncertainties, and t-ratios greater than two were obtained.

Table 6. Parameters identified from fitting the thermal models Eqs.(13-14).

Parameter	Unity	Model 1			Model 2		
		Value	Uncertainty	t-ratio	Value	Uncertainty	t-ratio
c_1	$\text{Wm}^{-2}\text{K}^{-1}$	-0.3200	0.1976	1.62	-	-	-
c_2	$\text{Wm}^{-2}\text{K}^{-2}$	-0.0088	0.0030	2.91	-0.01349	0.00078	17.3
c_5	$\text{Jm}^{-2}\text{K}^{-1}$	-9102	3253	2.80	-8931	3232	2.76

Table 7 summarizes the model's robustness. The ME, MAE, and the RMSE values are shown for both thermal models. It can be observed that similar values were obtained with a MAE error lower than 4%. From the ME values it can be seen that both models tend to slightly overestimate the power output. The same RMSE value 0.57% was obtained for both models, which indicates that both models reproduced the thermal behaviour of the prototype.

On the other hand, the percentage of $\pm 5\%$ error values, when considering the model and experimental uncertainties, were found to be slightly better for Model 2, moreover, 100% of the data series are within $\pm 10\%$ error for both models. For a graphical comparison between experimental and model values see Figs. 10(a-b).

Table 7. Experimental and simulation comparison analyses.

Residual coefficients	Model 1	Model 2
ME [%]	-0.54	-0.66
MAE[%]	3.93	3.83
RMSE[%]	0.57	0.57
Percentage series within $\pm 5\%$ error considering uncertainties [%]	96.8	100
Percentage series within $\pm 10\%$ error considering uncertainties [%]	98.9	100

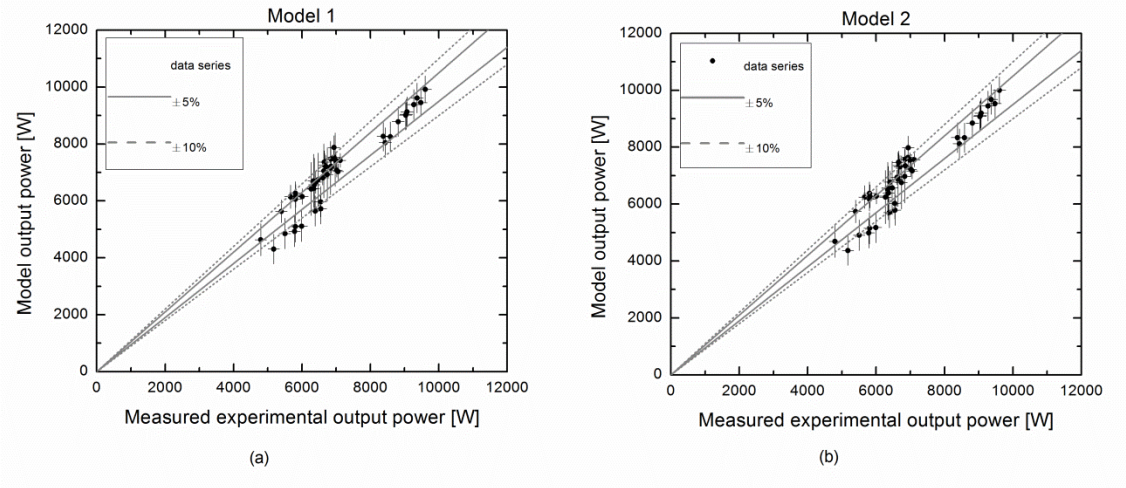


Fig. 10. Experimental output power versus thermal models power at a working temperature greater than the ambient.

6. Conclusions

This study tested a variable geometry solar collector for medium temperature applications, the CCStaR V1 prototype. Unlike previous studies, ray-tracing tools are used to introduce the beam and diffuse efficiencies as independent variables in the energy balance equation for a WLS adjustment.

The first step consisted of performing a simple geometrical characterization to determine the real position between the receiver tubes and the parabolas, and a ± 1 mm tolerance proved to be sufficient. Then, a ray-tracing model was validated using data series at ambient temperature, and the heat removal factor was determined with low uncertainty. Once the optical model is validated, data series at a temperature greater than the ambient temperature were used to determine the loss heat coefficients. Two thermal models were analysed, and both showed great agreement with experimental values, although only the second model gave results in t-ratios greater than two for the

curve parameters. It should also be noted that the c_5 coefficient could have a high relative uncertainty, as the variations in the dt_m/dt are not easily obtained for a solar concentrating collector because it operates normally with direct solar irradiation, which implicates that the test during cloudy days would not provide representative data. Thus, t-ratios greater than two could be acceptable for concentrating collectors of medium range temperature.

This study has proved that combining ray-tracing tools with experimental data is a useful method to determine the energy equation balance of large solar concentrators. The main advantage is that measurement of thermal efficiency at normal incidence is not required, and it can be applied for in situ measurements of large-scale solar thermal collectors.

Acknowledgements

This work was co-funded by the *Conselleria d'Economia, Hisenda i Innovació del Govern de les Illes Balears (Projecte Tractor, ParcBit)*, the *Universitat de les Illes Balears*, and *Tecnología Solar Concentradora, S.L.* We would like to give them all our heartfelt thanks.

References

- [1] Abbas, R., Muñoz-Antón, J., Valdés, M., Martínez-Val, J.M., High concentration linear Fresnel reflectors, *Energy Convers Manage* 72 (2013) 60-68. doi: <http://dx.doi.org/10.1016/j.enconman.2013.01.039>.
- [2] Russell, J.L., DePlomb, E.P., Bansal, R.K., Principles Of The Fixed Mirror Solar Concentrator. 2nd ed., General Atomic Co., San Diego, CA, Report No. GA-A12903. (1974) 139-145.
- [3] El-Refaie, M.F., Performance analysis of the stationary-reflector/tracking-absorber solar collector, *Appl. Energy* 28 (1987) 163-189. doi: [http://dx.doi.org/10.1016/0306-2619\(87\)90050-X](http://dx.doi.org/10.1016/0306-2619(87)90050-X).
- [4] Avila-Marin, A.L., Fernandez-Reche, J., Tellez, F.M., Evaluation of the potential of central receiver solar power plants: Configuration, optimization and trends, *Appl. Energy* 112 (2013) 274-288. doi: <http://dx.doi.org/10.1016/j.apenergy.2013.05.049>.
- [5] Weiss, W., Rommel, M., State of the Art within Task 33/IV. Subtask C. Solar Heat for Industrial Processes. Medium Temperature Collectors (2005).
- [6] Häberle, A., Berger, M., Luginsland, F., Zahler, C., Baitsch, M., Henning, H.-M., Rommel, M., Experience with linear concentrating Fresnel collectors for process heat applications Solar Paces, 14th International Symposium on Concentrating Solar Power and Chemical Energy Technologies (2008) Las Vegas, U.S.A.; March 4 – 7.

- 615 [7] Weiss, W., Rommel, M., Processes Heat Collectors. State of the Art within Task
616 33/IV (2008) Available at: <http://archive.iea-shc.org/publications/task.aspx?Task=33>.
- 617 [8] CEN, Thermal Solar Systems and Components - Solar Collectors - Part 2: Test
618 Methods, European Standard EN 12975-2:2006. European Committee for
619 Standardisation (2006).
- 620 [9] ISO, Solar energy -- Solar thermal collectors -- Test methods, ISO (Ed.) ISO
621 9806:2013(E) (2013).
- 622 [10] ASTM, Standard Test Method for Determining Thermal Performance of Tracking
623 Concentrating Solar Collectors, ASTM E 905-87 (1987).
- 624 [11] ASHRAE, Methods of testing to determine the thermal performance of solar
625 collectors, ASHRAE 93. American Society of Heating, Refrigerating and Air-
626 Conditioning Engineers, Inc. (2010).
- 627 [12] Jaramillo, O.A., Venegas-Reyes, E., Aguilar, J.O., Castrejón-García, R., Sosa-
628 Montemayor, F., Parabolic trough concentrators for low enthalpy processes, Renewable
629 Energy 60 (2013) 529-539. doi: <http://dx.doi.org/10.1016/j.renene.2013.04.019>.
- 630 [13] Nkwetta, D.N., Smyth, M., The potential applications and advantages of powering
631 solar air-conditioning systems using concentrator augmented solar collectors, Appl.
632 Energy 89 (2012) 380-386. doi: <http://dx.doi.org/10.1016/j.apenergy.2011.07.050>.

- 633 [14] Xu, L., Wang, Z., Li, X., Yuan, G., Sun, F., Lei, D., Dynamic test model for the
634 transient thermal performance of parabolic trough solar collectors, *Solar Energy* 95
635 (2013) 65-78. doi: <http://dx.doi.org/10.1016/j.solener.2013.05.017>.
- 636 [15] Pino, F.J., Caro, R., Rosa, F., Guerra, J., Experimental validation of an optical and
637 thermal model of a linear Fresnel collector system, *Appl. Therm. Eng.* 50 (2013) 1463-
638 1471. doi: <http://dx.doi.org/10.1016/j.applthermaleng.2011.12.020>.
- 639 [16] Kong, W., Wang, Z., Li, X., Li, X., Xiao, N., Theoretical analysis and experimental
640 verification of a new dynamic test method for solar collectors, *Solar Energy* 86 (2012)
641 398-406. doi: <http://dx.doi.org/10.1016/j.solener.2011.10.011>.
- 642 [17] Amrizal, N., Chemisana, D., Rosell, J.I., Barrau, J., A dynamic model based on the
643 piston flow concept for the thermal characterization of solar collectors, *Appl. Energy* 94
644 (2012) 244-250. doi: <http://dx.doi.org/10.1016/j.apenergy.2012.01.071>.
- 645 [18] Sallaberry, F., Pujol-Nadal, R., Martínez-Moll, V., Torres, J., Optical and thermal
646 characterization procedure for a variable geometry concentrator: A standard approach,
647 *Renewable Energy* 68 (2014) 842-852. doi:
648 <http://dx.doi.org/10.1016/j.renene.2014.02.040>.
- 649 [19] Draper, N.R., Smith, H., NetLibrary, I., *Applied regression analysis* (1998) 706.
- 650 [20] Souka, A.F., Safwat, H.H., Determination of the optimum orientations for the
651 double-exposure, flat-plate collector and its reflectors, *Solar Energy* 10 (1966) 170-174.
652 doi: 10.1016/0038-092X(66)90004-1.

653 [21] Pujol-Nadal, R., Martínez-Moll, V., Optical characterization of a fixed mirror solar
654 concentrator prototype by the ray-tracing procedure, J. Renewable Sustainable Energy
655 6 (2014) 043105-1-14. doi: <http://dx.doi.org/10.1063/1.4890219>.

656 [22] Russell, J.L., Jr., Investigation of a central station solar power plant. General
657 Atomic Company Report GA-A12759, August 31, (1973).

658 [23] Pujol Nadal, R., Martínez Moll, V., Optical analysis of the fixed mirror solar
659 concentrator by forward ray-tracing procedure., J Sol Energy Eng 134 (2012) 031009-1-
660 14. doi: 10.1115/1.4006575.

661 [24] Balasubramanian, V., Sankarasubramanian, G., Stretched tape design of fixed
662 mirror solar concentrator with curved mirror elements., Sol Energy 51 (1993) 109-119.
663 doi: 10.1016/0038-092X(93)90073-W.

664 [25] Pujol Nadal, R., Comportamiento óptico y térmico de un concentrador solar lineal
665 con reflector estacionario y foco móvil. (2012). PhD thesis. Available at:
666 <http://hdl.handle.net/10803/84115>. University of Balearic Islands. Departament de
667 Física.

668 [26] Pujol Nadal, R., Martínez Moll, V., Optical analysis of a curved-slats fixed-mirror
669 solar concentrator by a forward ray-tracing procedure, Appl. Opt. 52 (2013) 7389-7398.
670 doi: 10.1364/AO.52.007389.

671 [27] Pujol-Nadal, R., Martínez-Moll, V., Moià-Pol, A., Parametric Analysis of the
672 Fixed Mirror Solar Concentrator for Medium Temperature Applications, ASME
673 J. Solar Energy Eng. 136 (2014) 011011-1-7. doi: 10.1115/1.4026098.

- 674 [28] Pujol-Nadal, R., Martínez-Moll, V., Parametric analysis of the curved slats fixed
675 mirror solar concentrator for medium temperature applications, Energy Conversion and
676 Management 78 (2014) 676-683. doi:
677 <http://dx.doi.org/10.1016/j.enconman.2013.11.032>.
- 678 [29] Duffie, J.A., Beckman, W., Solar engineering of thermal processes., 2nd ed.,
679 Wiley, New York, 1991.
- 680 [30] ISO/IEC, Uncertainty of measurement - Part 3: Guide to the expression of
681 uncertainty in measurement (GUM:1995), ISO/IEC Guide 98-3:2008 (2008).
- 682 [31] Pettit, R.B., Vittitoe, C.N., Biggs, F., Simplified Computational Procedure for
683 Determining the Amount of Intercepted Sunlight in an Imaging Solar Concentrator.,
684 Journal of Solar Energy Engineering, Transactions of the ASME 105 (1983) 101-107.
685 doi: doi:10.1115/1.3266335.
- 686 [32] Buie, D., Dey, C.J., Bosi, S., The effective size of the solar cone for solar
687 concentrating systems., Solar Energy 74 (2003) 417-427. doi:
688 [http://dx.doi.org/10.1016/S0038-092X\(03\)00156-7](http://dx.doi.org/10.1016/S0038-092X(03)00156-7).
- 689 [33] Tesfamichael, T., Wäckelgård, E., Angular solar absorptance and incident angle
690 modifier of selective absorbers for solar thermal collectors., Solar Energy 68 (2000)
691 335-341. doi:10.1016/S0038-092X(00)00029-3
- 692 [34] Martínez Moll, V., Moià Pol, A., Pujol Nadal, R., Innovative Fixed Mirror Solar
693 Concentrator for Process Heat 2 (2008) 1177-1192EUROSUN 2008: 1st International
694 Conference on Solar Heating, Cooling and Buildings.

695 [35] Sallaberry, F., Pujol-Nadal, R., Jalón, A. G. de, & Martínez-Moll, V. (2015).
 696 Towards a Standard Testing Methodology for Medium-temperature Solar Collectors
 697 with Variable Geometry: : The direct radiation incidence angle modifier issue. Sol
 698 Energy 2015. Solar Energy 2015. <http://dx.doi.org/10.1016/j.solener.2015.05.029>.

699 [36] Rojas, E., Zarza, E., Fernández-García, A., González, L., Towards a standardized
 700 characterization of parabolic trough collectors (2008)2008 14th Biennial CSP
 701 SolarPACES Symposium March 4-7, 2008, Las Vegas, Nevada. CD U(CD-550-42709).

702